Research Article

Dolat Khan*, Mostafa A. Hussien, Awatif M. A. Elsiddieg, Showkat Ahmad Lone, and Ahmed M. Hassan

Exploration of generalized two-phase free convection magnetohydrodynamic flow of dusty tetra-hybrid Casson nanofluid between parallel microplates

https://doi.org/10.1515/ntrev-2023-0102
received May 6, 2023; accepted July 12, 2023

Abstract: Dusty Casson fluids and tetra-hybrid nanofluids are complex phenomena that find their extensive uses in engineering and industrial applications. For instance, dusty fluids are used in gas-freezing systems and nuclear power reactors. The main objective of this article is to focus on the characterization of generalized two-phase free convection magnetohydrodynamic flow of dusty tetra-hybrid Casson nanofluid among parallel microplates: dusty Casson fluid and tetra-hybrid nanofluid exhibit free movement and electrical conductivity. The Caputo–Fabrizio fractional derivative recently discovered generalizes the partial differential equations governing the flow. Highly accurate temperature and velocity distributions can be obtained using finite sine Fourier and Laplace transform together. This study examines the relationships between temperature, dust particle velocity, and Casson fluid velocity, along with the effects of magnetic parameter, Grashof number, dusty fluid parameter, Peclet number, Reynold number, and particle mass parameter. The Mathcad-15 software provides Casson, dusty, and temperature profiles graphically. The Nusselt number and skin friction are also examined for the tetra-hybrid nanofluid. The fractional Casson fluid model is more accurate than the classical model in terms of velocity, temperature, heat transfer, and skin friction. Graphical results conclude that the fractional Casson fluid model describes a more realistic aspect of both (fluid and dust particle) velocities and temperature profiles, heat transfer rate, and skin friction than the classical Casson fluid model. Furthermore, the heat transfer rate enhanced from 0 to 39.3111% of the tetra-hybrid nanofluid.

Keywords: tetra-hybrid nanofluid, two-phase flow, finite sine Fourier transform, dusty fluid, MHD, Laplace transform, Caputo–Fabrizio derivative

*** Corresponding author: Dolat Khan,** Faculty of Science, King Mongkut's University of Technology Thonburi (KMUTT), 126 Pracha Uthit Rd., Bang Mod, Thung Khru, Bangkok, 10140, Thailand, e-mail: dolat.ddk@gmail.com
Mostafa A. Hussien: Mechanical Engineering Department, College of Engineering, King Khalid University, Abha, 61421, Saudi Arabia
Awatif M. A. Elsiddieg: Department of Mathematics, College of Science and Humanities in Hotat Bani Tamim, Prince Sattam Bin Abdulaziz University, Al-Kharj, 11942, Saudi Arabia
Showkat Ahmad Lone: Department of Basic Sciences, College of Science and Theoretical, Studies, Saudi Electronic University, Jeddah-M, Riyadh, 11673, Saudi Arabia
Ahmed M. Hassan: Faculty of Engineering, Future University in Egypt, New Cairo, Egypt

Nomenclature

A	variable temperature.
T_{d}	ambient temperature
A_1	Rivlin–Ericksen tensor of the first kind
τ	time
B_0	applied magnetic field
u_1	velocity of the base fluid
c_{p}	specific heat capacity of fluid
u_0	constant velocity
Cf	skin friction
u_2	velocity of the particle
CF	Caputo–Fabrizio
Re	Reynolds number
d	distance between parallel plates
ρ	fluid density
Gr	Grashof number
μ	dynamic viscosity
g	gravitational acceleration
υ	kinematic viscosity
$H(t)$	heaviside step function

σ	electrical conductivity
I	identity tensor
α	fractional parameter
$J \times B$	Lorentz forces
β	Casson fluid parameter
K	dusty fluid parameter
β_{T}	coefficient of thermal expansion
k	thermal conductivity of the fluid
$\rho\vec{b}$	body forces
K_0	Stock's resistance coefficient
τ_{ij}	Cauchy stress tensor
M	non-dimensional magnetic parameter
θ	dimensionless temperature of the fluid
$N(\alpha)$	normalization function
N_0	number density of the dust particles
Nu	Nusselt number
P	pressure
Pe	Peclet number
P_{m}	particles' mass parameter
p_{y}	yield stress
$\vec{s}$	surface forces
T	temperature of the fluid
T_{w}	temperature of the wall

1 Introduction

A Casson fluid has an infinite viscosity at zero shear rates and no flow behavior below its yield stress [1]. Honey, hair, synthetic fibers, and soup are all Casson fluids. Oka [2] investigated the dynamics of Casson fluids in pipes. Mukhopadhyay and Mandal [3] studied the effect of Newtonian heating condition, mass, and heat transfer on the magnetohydrodynamics (MHD) flow of Casson fluid between two plates that were not stable. With its superior heat transmission, Casson fluid flow plays a crucial role in the confectionery industry [4]. Akbar and Khan [5] investigated the impact of a magnetic field on the peristaltic flow of Casson fluid in an asymmetric channel. Akbar [6] explored possible uses in refineries and crude oil processing using mathematical and graphical approaches. The entropy creation using the finite difference approach during thermal transport with nanoparticles of fractional Casson fluid in the presence of a magnetic field, radiation, and viscous dissipation was studied by Asjad *et al.* [8]. Noreen and Butt [7] looked at Casson fluid in physiological transit in a plumb conduit. Under the correct boundary and beginning circumstances, Nadeem *et al.* [9] also investigated the three-dimensional flow of a Casson nanofluid that conducts electricity. Recently, Khan *et al.* [10] investigated the effects of heat generation, chemical reactions, natural convection, and free convection on the flow of Casson fluids through a porous medium in a vertical channel. Using an explicit finite difference method, Reza-E-Rabbi *et al.* [11] studied the impact of Brownian motion and thermophoresis on the transport of a chemically reactive MHD Casson fluid through a stretched sheet. Due to the more realistic thinning component provided by non-Newtonian fluids, Casson fluids represent blood's rheological behavior in the cardiovascular system [12]. The radiative double diffusive Williamson hybrid nanofluid convection and mass transfer over a Riga surface are studied by Faisal *et al.* [13]. Asogwa *et al.* [14] examined the heat transfer characteristics of water-based Al_2O_3 nanoparticles, water-based CuO nanoparticles, and water-based Al_2O_3 nanoparticles on an exponentially accelerated radiative Riga plate surface. The governing partial differential equations (PDEs) are solved using the Laplace transform (LT) method. Volume fractions of nanoparticles may be anywhere from 1 to 4%, buoyancy forces can be anywhere from 5 to 20%, and the modified Hartmann number can be anywhere from 1 to 6.

Nanofluids are nanoparticle-suspended base fluids [15]. Nanofluids are promising for heat transfer applications in electronic devices, fuel cell technology, drug processes, hybrid-powered engines, engine combination/vehicle heat oversight, home refrigeration, chilling, domestic machining, and boiler flue heat reduction [16]. Hybrid pigments, attractive coatings, scratch-resistant coatings, anti-corrosion hair products, glass-inspired materials, sound and heat insulators, electrical insulators, fireproofing, intelligent textiles, green auto and dental products, hybrid anti-cancer nanoparticles, magnetic resonance imaging contrast agents, controlled-release biocapsules, biocatalysts, or photocatalyst actuators, optical chemical sensors, fuel cells, solar cells, biosensors, supercapacitors, bendable hybrid batteries, microlenses, and waveguides, color-changing coatings, and coatings are some of the numerous applications for organic–inorganic compounds of hybrid nanofluid [17]. Ramesh *et al.'s* [18] study delves into the impact of electromagnetic thermal expansion on the flow of a hybrid nanofluid comprising titanium oxide, iron oxide, and ethylene glycol. Tri-hybrid nanofluid is another name for the improved hybrid nanofluid. Tri-hybrid nanoparticles are composites of three nanofluids. Tri-hybrid nanoparticles are essential for increasing thermal conductivity. Composite particles may help electrical heaters, solar energy generation, nuclear safety, the pharmaceutical business, and others. Many scientists have studied tri-hybrid nanoparticles. The water-based ternary hybrid nanofluid flow dynamics in a three-dimensional computational domain – the impact of Dufour and Soret features – is reported by Bilal *et al.* [19]. The tetra-hybrid nanofluid [$(Al_2O_3-CuO-TiO_2-Ag)$/water] tetra thermal

efficiency in a magnetic field and with coupled convection across a vertically oriented cylinder is reported by Adnan *et al.* [20]. The thermophoretic particle deposition and the non-linear surface stretching-induced three-dimensional flow of nanofluid are studied by Asogwa *et al.* [21]. Zayan *et al.* [22] used a magnetic catheter to cross a narrowed artery, a non-uniform heat source (sink), and thermal radiation to form ternary hybrid nanostructures under the influence of thermal additives. The cross-tetra-hybrid nanofluid model initially developed by Tiwari and Das was re-formed by Sajid *et al.* [23].

Sunscreen, tennis balls, computers, microorganisms, medicine delivery, and cancer therapies are just some of the many applications of tetra-hybrid nanoparticles discussed in this section. The author also emphasizes the role of nanofluids, particularly tetraploids, in improving thermal conductivity and withstanding greater temperatures. This article describes the application of the Galerkin finite element method to the study of tetra-nanofluids, similarity transformations, thermal radiations, and the dissipation function in a converging/diverging channel. The author also highlights the need for sensitive nitrite electrochemical detection at the nanoscale, reporting on a polyaniline-linked tetra-amino cobalt phthalocyanine surface-functionalized ZnO hybrid nanomaterial. Using several spectroscopic methods, the researchers produced and studied the Schiff base molecule. They then used it to create a flame-resistant composite by incorporating it into a polypropylene matrix, as reported by Li *et al.* [24]. A novel nanofluid with Al_2O_3, CuO, TiO_2, and Ag nanoparticles dispersed in water was studied for thermal performance. Magnetic fields and permeability affect the thermal efficiency of nanofluid and the vertically aligned cylinder's combined convection, as investigated by Adnan *et al.* [20]. In fluid mechanics, multi-phase flow occurs when two or more thermodynamic phases of materials are in motion. Two-phase flows, which might be liquid–liquid, solid–liquid, solid–gas, or gas–liquid, are the most basic kinds of multi-phase flows [25]. Fluidization, nuclear reactors, dust cooling systems, and MHD generators are a few uses for multi-phase MHD flows. An example of a multi-phase flow that occurs naturally in humans is blood circulation. To better understand the heat transfer properties and multi-phase flow of a long gravity-assisted heat pipe, Chen *et al.* [26] undertook an experimental investigation. Several methods exist for determining the void ratio. Radiation attenuation [27,28], ultrasonic [29,30], impedance technique using capacitance [31], wire mesh sensors [32], and open and shut valves to measure volume [33] are the most often used methods. For further information, see the linked publications [34,35].

Fractional derivatives offer a more comprehensive understanding of complex phenomena that classical derivatives fail to capture. By incorporating fractional orders, these derivatives enable us to analyze and describe intricate processes such as fractals, anomalous diffusion, and non-local effects, thus expanding our knowledge beyond the limitations of classical calculus. To better understand and describe the world around us, Riemann-Liouville [36] was the first to use fractional derivatives. Despite useless variables in LT, the Riemann-Liouville (R-L) fractional derivative is helpful in a wide range of physical systems owing to two distinguishing qualities. The literature sometimes suggests the Caputo fractional derivative to fix the R-L fractional derivative. The Caputo fractional derivative applies to various physical issues in economics, chemistry, and physics. Research in several fields, including signal processing, diffusion, image processing, material mechanics, damping, pharmacokinetics, and bioengineering, might benefit from computational fluid dynamics (CFD) [37,38]. However, owing to a singularity in the CFD kernel, it is not feasible to accurately forecast the effects of some materials with significant heterogeneities. Several studies have covered the singularity problem in CFD [39]; to address this, Caputo–Fabrizio has presented a new definition with a non-singular kernel [40]. Furthermore, the analysis of the finite difference method is used for numerical research of fractional Maxwell nanofluids between two coaxial cylinders by Asjad *et al.* [41]. Asjad *et al.* [42] reported an innovative study on the application of fractional partial differential equations in the context of MHD Casson fluid flow, which incorporates novel ternary nano-particles. LT solves the dimensionless governing model, and comparisons are shown from the answers. Instead of the symmetric qualities for various fractional parameters, other aspects of the issue have been examined. Ternary nanoparticles increase fluid characteristics better than hybrid and mono-nanoparticles. The law-based fractional model fits experimental data more accurately and efficiently than an artificial substitute. The second rule of MHD flow of a Casson nanofluid in a porous medium with sliding and ramping wall heating has recently been the subject of an innovative multi-fractional comparative study by Khan *et al.* [43]. The model was generalized using triple fractional definitions, and the solution was found using a combination of Laplace and Zakian's numerical approach. This research aimed to examine and contrast the findings obtained using the aforementioned three fractional operators in terms of entropy production, velocity profile, temperature profile, and Bejan number. Various physical characteristics were explored to maximize or minimize entropy formation.

A thorough review of the relevant literature demonstrates that despite the recent development of C-F time-fractional derivatives, no one has yet attempted to use them to obtain exact solutions for the flow of Casson fluid and tetra-hybrid nanofluid with dust particles and heat transfer between parallel plates. Despite all the research on the issue, no clear solution has emerged. We performed studies on the unsteady flow of Casson fluid, considering the presence of homogeneously spread dust particles, the effects of MHD, and the transfer of heat across parallel plates to fill this knowledge gap. We used a two-phase flow approach, modeling the fluid flow and particle motion momentum equations separately and then using the CF fractional derivative to generalize our results. We made use of Laplace and finite sine fourier transforms (FSFTs) to gain precise solution about the temperature as well as the velocity profiles. The Nusselt number was found by applying the energy equation to the problem, and the skin friction value was found using the momentum equation to the problem. In addition, we investigated the impacts of different embedded parameters on velocities, temperatures, skin friction, and Nusselt numbers, and we presented our results visually and in a tabular form.

2 Mathematical formulation

In the current flow regime, a viscoelastic Casson fluid with dusty particles and tetra-hybrid nanofluid flows unsteadily and incompressibly between two parallel vertical plates. As shown in Figure 1, the distance that separates the plates is denoted by the letter "*d*," and the velocity of the fluid is regarded to be in the *x*-direction. The flow field is subjected to a uniform and transverse magnetic field B_0 with the left plate remaining immobile and the right plate flowing at a constant speed. Both the velocity of the dust particles and the velocity of the Casson fluid are expressed by $u_1(\zeta, \tau)$ and $u_2(\zeta, \tau)$, respectively. The temperature of the plate on the right may be adjusted with variable temperature $T_d + (T_w - T_d)A\tau$, but the temperature of the plate on the left is denoted by T_d [43,44].

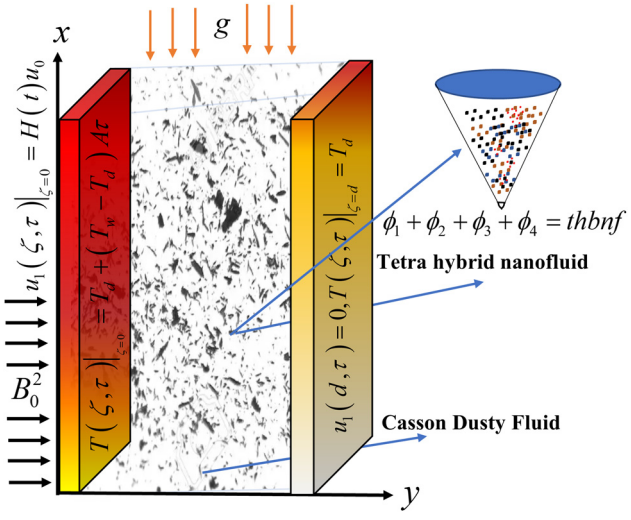

Figure 1: Illustrative diagram of the presented problem.

The constitutive equations for the Casson fluid are as follows [45]:

$$\nabla \cdot \boldsymbol{V} = 0, \tag{1}$$

$$\rho \frac{\mathrm{d}\boldsymbol{V}}{\mathrm{d}t} = \mathrm{div}(\boldsymbol{\tau}_{ij}) + \rho \cdot \boldsymbol{b} + \boldsymbol{s}, \tag{1.1}$$

where ρ, $\mathrm{d}/\mathrm{d}t$, $\boldsymbol{\tau}_{ij}$, $\rho \cdot \boldsymbol{b}$, and $\boldsymbol{s}$ are the fluid density, material time derivative, body forces, Cauchy stress tensor, and the interactive surface forces that generate due to the interaction between fluid particles and dust particles.

Using the Maxwell law, generalized Ohm's law, and Boussinesq's approximation, the body and surface forces in Eq. (4) become [45]

$$\begin{aligned} \rho \cdot \boldsymbol{b} &= J \times B + \rho g \beta_T (T - T_d) \\ &= -\sigma B_0^2 u_1 + g \rho \beta_T (T - T_d), \end{aligned} \tag{1.2}$$

$$\boldsymbol{s} = K_0 N_0 (u_2 - u_1). \tag{1.3}$$

Casson (1959) stated and derived the rheological equation for unsteady Casson fluid flow, which can be expressed as [45]:

$$\boldsymbol{\tau}_{ij} = \begin{Bmatrix} \left(\mu_\varepsilon \frac{p_y}{\sqrt{2\pi_1}}\right) 2e_{ij}, & \pi_1 > \pi_c \\ \left(\mu_\varepsilon \frac{p_y}{\sqrt{2\pi_c}}\right) 2e_{ij}, & \pi_1 > \pi_c \end{Bmatrix}, \tag{1.4}$$

where μ_ε shows the dynamic viscosity of the plastic non-Newtonian fluid $\mu_\varepsilon = \rho\upsilon$ and p_y shows the yield stress of the fluid, respectively, $\pi_1 = e_{ij}e_{ij}$, where e_{ij} is used to represent the component of the deformation rate for non-Newtonian fluid, and (i, j)th deformation rate component can be written as:

$$\boldsymbol{e}_{ij} = -p\boldsymbol{I} + \mu \boldsymbol{A}_1, \tag{1.5}$$

where P, $\boldsymbol{I}$, μ, and $\boldsymbol{A}_1$ are the indeterminate pressure, identity tensor, dynamic viscosity, and Rivlin–Ericksen tensor of the first kind.

$$\mathrm{div}(\tau_{ij}) = \left(\mu_\varepsilon \frac{p_y}{\sqrt{2\pi_1}}\right) \frac{\partial^2 u}{\partial y^2}. \tag{1.6}$$

When Equations (1.2)–(1.6) are utilized, Equation (1) becomes can be expressed in component form as [45]:

$$\frac{\rho_{\text{mthnf}}\partial u_1(\zeta,\tau)}{\partial\tau} = \left(1+\frac{1}{\lambda}\right)\mu_{\text{mthnf}}\frac{\partial^2 u_1(\zeta,\tau)}{\partial\zeta^2} - K_0N_0(u_1(\zeta,\tau)-u_2(\zeta,\tau)) - \sigma B_0^2 u_1(\zeta,\tau) + g(\rho\beta_{\text{T}})_{\text{mthnf}}(T-T_{\text{d}}). \tag{1.7}$$

The momentum equation of dust particles is given as [45]:

$$m\frac{\partial u_2(\zeta,\tau)}{\partial\tau} = K_0(u_1(\zeta,\tau)-u_2(\zeta,\tau)), \tag{2}$$

where m is the mass of dust particles and K_0 is Stock's resistance coefficient.

The energy equation of fluid is given as [45]:

$$\frac{(\rho c_{\text{p}})_{\text{mthnf}}}{k_{\text{mthnf}}}\frac{\partial T(\zeta,\tau)}{\partial\tau} = \frac{\partial^2 T(\zeta,\tau)}{\partial\zeta^2}. \tag{3}$$

Some physical conditions are as follows [45]:

$$\left.\begin{aligned} &u_1(\zeta,0)=0,\quad u_2(\zeta,0)=0,\ T(\zeta,0)=T_{\text{d}}, u_1(\zeta,\tau)|_{\zeta=0}=H(t)u_0\\ &u_1(d,\tau)=0, T(\zeta,\tau)|_{\zeta=0}=T_{\text{d}}+(T_{\text{w}}-T_{\text{d}})A\tau,\ T(\zeta,\tau)|_{\zeta=d}=T_{\text{d}}\end{aligned}\right\}, \tag{4}$$

where

$$\mu_{\text{mthnf}} = \frac{\mu_{\text{f}}}{(1-\phi_1)^{2.5}(1-\phi_2)^{2.5}(1-\phi_3)^{2.5}(1-\phi_4)^{2.5}},$$

$$\frac{\rho_{\text{mthnf}}}{\rho_{\text{f}}} = (1-\phi_4)\left[\left((1-\phi_3)((1-\phi_2)((1-\phi_1)+\phi_1\rho_{\text{s1}}/\rho_{\text{f}})+\phi_2\rho_{\text{s2}}/\rho_{\text{f}})+\phi_3\rho_{\text{s3}}/\rho_{\text{f}}\right)+\phi_4\rho_{\text{s4}}/\rho_{\text{f}}\right],$$

$$\frac{k_{\text{mthnf}}}{k_{\text{mhnf}}} = \frac{k_{\text{s4}}+2k_{\text{mhnf}}-2\phi_4(k_{\text{mhnf}}-k_{\text{s4}})}{k_{\text{s4}}+2k_{\text{mhnf}}+\phi_4(k_{\text{mhnf}}-k_{\text{s4}})},\quad \frac{k_{\text{mhnf}}}{k_{\text{hnf}}} = \frac{k_{\text{s3}}+2k_{\text{hnf}}-2\phi_3(k_{\text{hnf}}-k_{\text{s3}})}{k_{\text{s3}}+2k_{\text{hnf}}+\phi_3(k_{\text{hnf}}-k_{\text{s3}})}$$

$$\frac{k_{\text{hnf}}}{k_{\text{nf}}} = \frac{k_{\text{s2}}+2k_{\text{nf}}-2\phi_2(k_{\text{nf}}-k_{\text{s2}})}{k_{\text{s2}}+2k_{\text{nf}}+\phi_2(k_{\text{nf}}-k_{\text{s2}})},\quad \frac{k_{\text{nf}}}{k_{\text{f}}} = \frac{k_{\text{s1}}+2k_{\text{f}}-2\phi_1(k_{\text{f}}-k_{\text{s1}})}{k_{\text{s1}}+2k_{\text{f}}+\phi_1(k_{\text{f}}-k_{\text{s1}})}$$

$$\sigma_{\text{mthnf}} = \frac{\sigma_{\text{mhnf}}}{\sigma_{\text{s4}}},\quad \sigma_{\text{mhnf}} = \frac{\sigma_{\text{hnf}}}{\sigma_{\text{s3}}},\quad \sigma_{\text{hnf}} = \frac{\sigma_{\text{nf}}}{\sigma_{\text{s2}}},\quad \sigma_{\text{nf}} = \frac{\sigma_{\text{f}}}{\sigma_{\text{s1}}},$$

$$\frac{\sigma_{\text{mthnf}}}{\sigma_{\text{mhnf}}} = 1+\frac{3(\sigma_{\text{mhnf}}-1)\phi_4}{(\sigma_{\text{mhnf}}+2)-(\sigma_{\text{mhnf}}-1)\phi_4},\quad \frac{\sigma_{\text{mhnf}}}{\sigma_{\text{hnf}}} = 1+\frac{3(\sigma_{\text{hnf}}-1)\phi_3}{(\sigma_{\text{hnf}}+2)-(\sigma_{\text{hnf}}-1)\phi_3},$$

$$\frac{\sigma_{\text{hnf}}}{\sigma_{\text{nf}}} = 1+\frac{3(\sigma_{\text{nf}}-1)\phi_2}{(\sigma_{\text{nf}}+2)-(\sigma_{\text{nf}}-1)\phi_2},\quad \frac{\sigma_{\text{nf}}}{\sigma_{\text{f}}} = 1+\frac{3(\sigma_{\text{f}}-1)\phi_1}{(\sigma_{\text{f}}+2)-(\sigma_{\text{f}}-1)\phi_1},$$

$$\frac{(\rho c_{\text{p}})_{\text{mthnf}}}{(\rho c_{\text{p}})_{\text{f}}} = (1-\phi_4)\left[\left((1-\phi_3)\left(\begin{matrix}(1-\phi_2)((1-\phi_1)+\phi_1(\rho c_{\text{p}})_{\text{s1}}/(\rho c_{\text{p}})_{\text{f}})\\ +\phi_2(\rho c_{\text{p}})_{\text{s2}}/(\rho c_{\text{p}})_{\text{f}}\end{matrix}\right)+\phi_3(\rho c_{\text{p}})_{\text{s3}}/(\rho c_{\text{p}})_{\text{f}}\right)+\phi_4(\rho c_{\text{p}})_{\text{s4}}/(\rho c_{\text{p}})_{\text{f}}\right]$$

$$\frac{(\rho\beta_{\text{T}})_{\text{mthnf}}}{(\rho\beta_{\text{T}})_{\text{f}}} = (1-\phi_4)\left[\left((1-\phi_3)\left(\begin{matrix}(1-\phi_2)((1-\phi_1)+\phi_1(\rho\beta_{\text{T}})_{\text{s1}}/(\rho\beta_{\text{T}})_{\text{f}})\\ +\phi_2(\rho\beta_{\text{T}})_{\text{s2}}/(\rho\beta_{\text{T}})_{\text{f}}\end{matrix}\right)+\phi_3(\rho\beta_{\text{T}})_{\text{s3}}/(\rho\beta_{\text{T}})_{\text{f}}\right)+\phi_4(\rho\beta_{\text{T}})_{\text{s4}}/(\rho\beta_{\text{T}})_{\text{f}}\right].$$

Dimensionless variables are those that express quantities in a fashion that is independent of any specified units or scale, which are as follows:

$$\left.\begin{aligned} &u_1^* = \frac{u_1}{u_0},\ \tau^* = \frac{u_0}{d}\tau,\ \zeta^* = \frac{\zeta}{d},\ \theta^* = \frac{T-T_{\text{d}}}{T_{\text{w}}-T_{\text{d}}},\ \text{and } u_2^* = \frac{u_2}{u_0}\end{aligned}\right\}. \tag{5}$$

The dimensionless form was obtained by applying equations (5) to (1)–(4), which are as follows:

$$\text{Re}\frac{c_1\partial u_1(\zeta,\tau)}{\partial\tau} = c_2\lambda_1\frac{\partial^2 u_1(\zeta,\tau)}{\partial\zeta^2} - K(u_1(\zeta,\tau)-u_2(\zeta,\tau)) - Mu_1(\zeta,\tau) + \text{Gr}\theta(\zeta,\tau)\,, \tag{6}$$

$$\frac{\partial u_2(\zeta,\tau)}{\partial\tau} = P_{\text{m}}(u_1(\zeta,\tau)-u_2(\zeta,\tau)), \tag{7}$$

$$\frac{\partial\theta(\zeta,\tau)}{\partial\tau} = \frac{c_3}{c_4\,\mathrm{Pe}}\frac{\partial^2\theta(\zeta,\tau)}{\partial\zeta^2}. \tag{8}$$

The physical conditions represented in a dimensionless behavior are as follows:

$$\left.\begin{aligned} &u_1(\zeta,0) = 0,\ u_2(\zeta,0) = 0,\ T(\zeta,0) = T_\mathrm{d},\ u_1(\zeta,\tau)|_{\zeta=0} = H(t)\\ &u_1(d,\tau) = 0, T(\zeta,\tau)|_{\zeta=0} = \tau,\ T(\zeta,\tau)|_{\zeta=d} = 0 \end{aligned}\right\}, \tag{9}$$

$$\mathrm{Pe} = \frac{(\rho c_\mathrm{p})_\mathrm{mthnf}u_0 d}{k_\mathrm{mthnf}}, \mathrm{Gr} = \frac{g(\beta_\mathrm{T})_\mathrm{mthnf}d^2(T_\mathrm{w}-T_\mathrm{d})}{u_0\upsilon_\mathrm{mthnf}}, P_\mathrm{m} = \frac{K_0 d}{mu_0}, K = \frac{K_0N_0d^2}{(\rho\upsilon)_\mathrm{mthnf}}, \mathrm{Re} = \frac{u_0 d}{\upsilon_\mathrm{mthnf}}, M = \frac{\sigma_\mathrm{mthnf}B_0^2d^2}{(\rho\upsilon)_\mathrm{mthnf}},$$

$$\lambda_1 = 1+\frac{1}{\lambda}, c_1 = (1-\phi_4)\left[\left((1-\phi_3)((1-\phi_2)((1-\phi_1)+\phi_1\rho_{s1}/\rho_\mathrm{f})+\phi_2\rho_{s2}/\rho_\mathrm{f})+\phi_3\rho_{s3}/\rho_\mathrm{f}\right)+\phi_4\rho_{s4}/\rho_\mathrm{f}\right]$$

$$c_2 = \frac{1}{(1-\phi_1)^{2.5}(1-\phi_2)^{2.5}(1-\phi_3)^{2.5}(1-\phi_4)^{2.5}},\ c_3 = \frac{k_{s4}+2k_\mathrm{mhnf}-2\phi_4(k_\mathrm{mhnf}-k_{s4})}{k_{s4}+2k_\mathrm{mhnf}+\phi_4(k_\mathrm{mhnf}-k_{s4})},$$

$$c_4 = (1-\phi_4)\left[\left((1-\phi_3)((1-\phi_2)((1-\phi_1)+\phi_1(\rho c_\mathrm{p})_{s1}/(\rho c_\mathrm{p})_\mathrm{f})+\phi_2(\rho c_\mathrm{p})_{s2}/(\rho c_\mathrm{p})_\mathrm{f})+\phi_3(\rho c_\mathrm{p})_{s3}/(\rho c_\mathrm{p})_\mathrm{f}\right)+\phi_4(\rho c_\mathrm{p})_{s4}/(\rho c_\mathrm{p})_\mathrm{f}\right]$$

$$c_5 = (1-\phi_4)\left[\left((1-\phi_3)\left((1-\phi_2)((1-\phi_1)+\phi_1(\rho\beta_\mathrm{T})_{s1}/(\rho\beta_\mathrm{T})_\mathrm{f})+\phi_2(\rho\beta_\mathrm{T})_{s2}/(\rho\beta_\mathrm{T})_\mathrm{f}\right)\right.\right. \tag{10}$$
$$\left.\left.+\phi_3(\rho\beta_\mathrm{T})_{s3}/(\rho\beta_\mathrm{T})_\mathrm{f}\right)+\phi_4(\rho\beta_\mathrm{T})_{s4}/(\rho\beta_\mathrm{T})_\mathrm{f}\right].$$

The C-F time-fractional parameter α on equations (6)–(8) yields the following:

$$c_1\,\mathrm{Re}\,{}^{CF}D_\tau^\alpha u_1(\zeta,\tau) = c_2\lambda_1\frac{\partial^2u_1(\zeta,\tau)}{\partial\zeta^2} - K(u_1(\zeta,\tau)-u_2(\zeta,\tau)) - Mu_1(\zeta,\tau)+\mathrm{Gr}\theta(\zeta,\tau), \tag{11}$$

$${}^{\mathrm{CF}}D_\tau^\alpha u_2(\zeta,\tau) = P_\mathrm{m}(u_1(\zeta,\tau)-u_2(\zeta,\tau)), \tag{12}$$

$${}^{\mathrm{CF}}D_\tau^\alpha\frac{c_4\mathrm{Pe}}{c_3}\theta(\zeta,\tau) = \frac{\partial^2\theta(\zeta,\tau)}{\partial\zeta^2}. \tag{13}$$

In this context, the C-F time-fractional operator with fractional parameter is denoted by ${}^{\mathrm{CF}}D_\tau^\alpha$, and its definition is given as follows [43,44]:

$${}^{\mathrm{CF}}D_\tau^\alpha\psi(\tau) = N(\alpha)(1-\alpha)^{-1}\int_0^\tau \exp(-\alpha(t-\tau)(1-\alpha)^{-1})\psi'(\tau)\mathrm{d}(\tau). \tag{14}$$

That is, $N(0) = N(1) = 1$, $\alpha\in(0,1)$.

It can be shown from [44] that the Laplace transformation for the C-F fractional derivative of order $0<\alpha\le 1$ and $m\in N$ is as follows:

$$\left.\begin{aligned} &L({}^{\mathrm{CF}}D_{m+\alpha}^\tau\psi(\tau))(q) = \frac{1}{1-\alpha}L(\psi^{(m+1)}(\tau))L\left(\exp\left(-\frac{\alpha}{1-\alpha}\tau\right)\right) = \frac{s^{m+1}L(\psi(\tau)-q^m\psi(0)-q^{m-1}\psi'(0)-\psi^m(0))}{q+\alpha(1-q)}\\ &\text{In particular case:}\\ &L({}^{\mathrm{CF}}D_\alpha^\tau(u_1(\zeta,\tau),q)) = \frac{qL(u_1(\zeta,\tau))}{q+\alpha(1-q)}, m=0, \end{aligned}\right\} \tag{15}$$

3 Exact solutions to the problem

Joint Laplace and FSFTs solve fractional PDEs exactly.

3.1 Calculation of temperature

If we solve Eq. (13) using the LT, we obtain the following:

$$\frac{q\, n_0 \mathrm{Pe}}{q + n_1}\bar{\theta}(\zeta, q) = \frac{d^2\bar{\theta}(\zeta, q)}{\partial\zeta^2}. \tag{16}$$

In a similar vein, Eq. (18) may also be rewritten as:

$$\left.\begin{aligned} &\overline{u}_1(\zeta, 0) = 0, \quad \overline{u}_2(\zeta, 0) = 0, \quad \overline{T}(\zeta, 0) = 0, \overline{u}_1(\zeta, q)|_{\zeta=0} = H(q) \\ &\overline{u}_1(1, q) = 0, \quad \overline{T}(\zeta, q)|_{\zeta=0} = \frac{1}{q^2}, \quad \overline{T}(\zeta, q)|_{\zeta=1} = 0 \end{aligned}\right\}. \tag{17}$$

Taking both sides of Eq. (16) $\int_0^d$ w.r.t ζ and also multiplying $\sin(n\pi)$, we obtain the following:

$$\int_0^d \left(\frac{q\, n_0 \mathrm{Pe}}{q + n_1}\bar{\theta}(\zeta, q)\sin(n\pi)\right)\mathrm{d}\zeta = \int_0^d \left(\frac{d^2\bar{\theta}(\zeta, q)}{\partial\zeta^2}\sin(n\pi)\right)\mathrm{d}\zeta. \tag{18}$$

Now, in Eq. (18), applying the FSFT and using the initial conditions (ICs) and boundary conditions (BCs), we obtain the following:

$$\bar{\theta}_{\mathrm{FSFT}}(\eta, q) = \frac{A_1}{q^2}(q + n_1)(q + A_2)^{-1}. \tag{19}$$

A better way to write Eq. (19) is as:

$$\begin{aligned} \bar{\theta}_{\mathrm{FSFT}}(\eta, q) = {} & A_1 A_2^{-2}(n_1 - A_2)(A_2 + q)^{-1} \\ & - \frac{A_1(n_1 - A_2)A_2^{-2}}{q} + \frac{n_1 A_1 A_2^{-1}}{q^2}. \end{aligned} \tag{20}$$

The inverted LT of Eq. (20) may be expressed as follows:

$$\theta_{\mathrm{FSFT}}(\eta, \tau) = A_3 \exp(-A_2\, \tau) - A_3 + n_1 A_1 A_2^{-1}\, \tau. \tag{21}$$

By inversing FSFT of Eq. (21), we find the following optimal temperature profile:

$$\theta(\zeta, \tau) = (1 - \zeta)\, \tau + 2\sum_{n=1}^{\infty}(A_3(1 + \exp(-A_2\tau))\sin(n\pi\zeta), \tag{22}$$

$$\begin{aligned} & n_0 = \frac{1}{1 - \alpha}, n_1 = \frac{\alpha}{1 - \alpha}, A_1 = \frac{n\pi}{\mathrm{Pe}\, n_0 + (n\pi)^2}, \\ & A_2 = \frac{(n\pi)^2\, n_1}{\mathrm{Pe}\, n_0 + (n\pi)^2}, A_3 = A_1(n_1 - A_2)A_2^{-2}. \end{aligned} \tag{23}$$

By taking the LT from Eq. (12) and plugging it into Eq. (17), we obtain the following:

$$\left.\begin{aligned} & q n_0(q + n_1)^{-1}\overline{u}_2(\zeta, q) = P_{\mathrm{m}}(\overline{u}_1(\zeta, q) - \overline{u}_2(\zeta, q)) \\ & P_{\mathrm{m}}\overline{u}_1(\zeta, q) = \left(\frac{q\, n_0}{(q + n_1)}\right)\overline{u}_2(\zeta, q) + \overline{P_{\mathrm{m}}u_2}(\zeta, q) \\ & P_{\mathrm{m}}\overline{u}_1(\zeta, q) = \left(\left(\frac{q\, n_0}{(q + n_1)}\right) + P_{\mathrm{m}}\right)\overline{u}_2(\zeta, q) \\ & P_{\mathrm{m}}\overline{u}_1(\zeta, q) = \left(\left(\frac{q\, n_0}{P_{\mathrm{m}}(q + n_1)}\right) + 1\right)\overline{u}_2(\zeta, q) \end{aligned}\right\}. \tag{24}$$

Finally, the momentum equation for dust particles is as follows:

$$\overline{u}_2(\zeta, \tau) = \left(\frac{q + n_1}{n_2(q + n_3)}\right)\overline{u}_1(\zeta, \tau), \tag{25}$$

where

$$n_2 = \frac{P_{\mathrm{m}} + n_0}{P_{\mathrm{m}}}, \text{ and } n_3 = \frac{P_{\mathrm{m}} n_1}{n_0 + P_{\mathrm{m}}}. \tag{26}$$

3.2 Solution of the velocity profile

By applying the modification [44], we obtain the following:

$$u_1(\zeta, \tau) = (1 - \zeta)H(\tau) + \overline{\Re}(\zeta, \tau). \tag{27}$$

The following results from applying Eqs. (11) to (27):

$$\begin{aligned} & \mathrm{Re}c_1({}^{\mathrm{CF}}D_\tau^a((1 - \zeta)H(\tau) + \overline{\Re}(\zeta, \tau))) \\ & = \left\{\begin{aligned} & \lambda_1 c_2 \frac{\partial^2}{\partial\zeta^2}((1 - \zeta)H(\tau) + \overline{\Re}(\zeta, \tau)) \\ & + K\left(\frac{u_2(\zeta, \tau)}{((1 - \zeta)H(\tau) + \overline{\Re}(\zeta, \tau))} - 1\right) \\ & \cdot((1 - \zeta)H(\tau) + \overline{\Re}(\zeta, \tau)) + \mathrm{Gr}\theta(y, t) \\ & - M((1 - \zeta)H(\tau) + \overline{\Re}(\zeta, \tau)) \end{aligned}\right\}. \end{aligned} \tag{28}$$

By incorporating the modified ICs and BCs, we obtain the following:

$$\overline{\Re}(\zeta, 0) = 0, \ \overline{\Re}(0, \tau) = 0, \ \overline{\Re}(1, \tau) = 0. \tag{29}$$

The following results are obtained after applying the LT to Eqs. (28) and (29):

$$\begin{aligned} & \frac{\mathrm{Re}n_0 c_1 q}{q + n_1}\overline{\Re}(\zeta, q) + \frac{\mathrm{Re}n_0 c_1 q}{q + n_1}(1 - \zeta)H(q) \\ & = \left\{\begin{aligned} & \lambda_1 c_2 \frac{\mathrm{d}^2}{\mathrm{d}\zeta^2}\overline{\Re}(\zeta, q) + K\left\{\left(\frac{q + n_1}{n_2(q + n_3)}\right)\right. \\ & \left. - 1\right\}(\overline{\Re}(\zeta, q) + (1 - \zeta)H(q)) \\ & - M\overline{\Re}(\zeta, q) - M(1 - \zeta)H(q) + \mathrm{Gr}\bar{\theta}(\zeta, q) \end{aligned}\right\}, \end{aligned} \tag{30}$$

$$\left(\frac{\mathrm{Re}n_0c_1q}{q+n_1}-\lambda_1c_2\frac{\mathrm{d}^2}{\mathrm{d}\zeta^2}-K\left\{\left(\frac{q+n_1}{n_2(q+n_3)}\right)-1\right\}+M\right)\overline{\Re}(\zeta,q)$$
$$=\left\{\left(K\left\{\left(\frac{q+n_1}{n_2(q+n_3)}\right)-1\right\}-\frac{\mathrm{Re}n_0c_1q}{q+n_1}-M\right)(1-\zeta)H(q)+\mathrm{Gr}\bar{\theta}(\zeta,q)\right\}. \quad (31)$$

Obtain the Fourier sine transform (FSFT) of Eq. (31) and simplify it as follows

$$\overline{\Re}_{\mathrm{FSFT}}(\eta,q)=\left(\frac{q^2-n_4\,q-n_5}{q^2+A_4\,q+A_5}\right)(1-\eta)H(q)+\frac{\mathrm{Gr}\,n_2\,A_1}{q^2}\cdot\frac{(q+n_1)^2}{q+A_2}\cdot\frac{(q+n_3)}{q^2+A_4\,q+A_5}. \quad (32)$$

It is possible to rewrite Eq. (31) such that it is more understandable and correct as:

$$\overline{\Re}_{\mathrm{FSFT}}(\eta,q)=\left\{1-\frac{A_8}{q+A_6}+\frac{A_9}{q-A_7}\right\}(1-\eta)H(q)-\left\{\frac{A_{10}}{q^2}-\frac{A_{11}}{q}-\frac{A_{12}}{q+A_2}-\frac{A_{13}}{q+A_6}-\frac{A_{14}}{q-A_7}\right\}. \quad (33)$$

By inverting LT of Eq. (33), we obtain the following:

$$\overline{\Re}_{\mathrm{FSFT}}(\eta,\tau)=\begin{Bmatrix}\{H(\tau)-A_8\exp(-A_6\tau)*H(\tau)+A_9\exp(A_7\tau)\\ *H(\tau)\}(1-\eta)-A_{10}\tau+A_{11}+A_{12}\exp(-A_2\tau)\\ +A_{13}\exp(-A_6\tau)+A_{14}\exp(L_7\tau)\end{Bmatrix}. \quad (34)$$

After further simplification, Eq. (34) becomes

$$\overline{\Re}_{\mathrm{FSFT}}(\eta,\tau)=\{(1-A_8\exp(-A_6\tau)+A_9\exp(A_7\tau)*H(\tau))\}(1-\eta)-A_{10}\tau+A_{11}+A_{12}\exp(-A_2\tau)+A_{13}\exp(-A_6\tau)+A_{14}\exp(L_7\tau). \quad (35)$$

By inverting FSFT of Eq. (35), we obtain the following:

$$\overline{\Re}(\zeta,\tau)=2\sum_{n=1}^{\infty}\begin{Bmatrix}\{(1-A_8\exp(-A_6\tau)+A_9\exp(A_7\tau)\\ *H(\tau))\}(1-\eta)-A_{10}\tau+A_{11}\\ +A_{12}\exp(-A_2\tau)+A_{13}\exp(-A_6\tau)\\ +A_{14}\exp(L_7\tau)\end{Bmatrix}\times\sin(n\pi\zeta). \quad (36)$$

By substituting Eq. (36) into Eq. (27), we obtain the following:

$$u_1(\zeta,\tau)=(1-\zeta)H(\tau)+2\sum_{n=1}^{\infty}\begin{Bmatrix}\{(1-A_8\exp(-A_6\tau)+A_9\exp(A_7\tau)\\ *H(\tau))\}\times(1-\eta)-A_{10}\tau+A_{11}\\ +A_{12}\exp(-A_2\tau)+A_{13}\exp(-A_6\tau)\\ +A_{14}\exp(L_7\tau)\end{Bmatrix}\sin(n\pi\zeta). \quad (37)$$

Note: An important thing to keep in mind is that "*" represents the convolution product.

The validity of our obtained general solutions is shown by the fact that Eq. (37) fulfills the imposed boundary constraints.

3.3 Nusselt number

In mathematical terms, the dimensionless form of the Nusselt number can be expressed as

$$\mathrm{Nu}=-\frac{k_{\mathrm{mthnf}}}{k_{\mathrm{mhnf}}}\frac{\partial\theta(\zeta,\tau)}{\partial\zeta}\bigg|_{\zeta=0}. \quad (38)$$

3.4 Skin friction

Mathematically, the equation for the left-hand skin friction is as follows:

$$\mathrm{Cf}=c_2\frac{\partial u_1(\zeta,\tau)}{\partial\zeta}\bigg|_{\zeta=0}. \quad (39)$$

4 Graphical results and discussion

In this study, the authors investigate the unsteady flow of viscoelastic Casson dusty fluid and tetra-hybrid nanofluid in two parallel plates. The authors have also taken into account the impacts of heat transmission and MHD. To obtain precise answers, both LT and FSFT have been used. The tables and figures illustrate the influence that the various embedded parameters have on the velocities of the fluids as well as on the temperature distribution.

For this purpose, we draw up Figure 2(i) and (ii) to examine the effect of Casson fractional parameters and dusty fluid velocities by using the classical derivative that yields as a single velocity profile. However, the figures

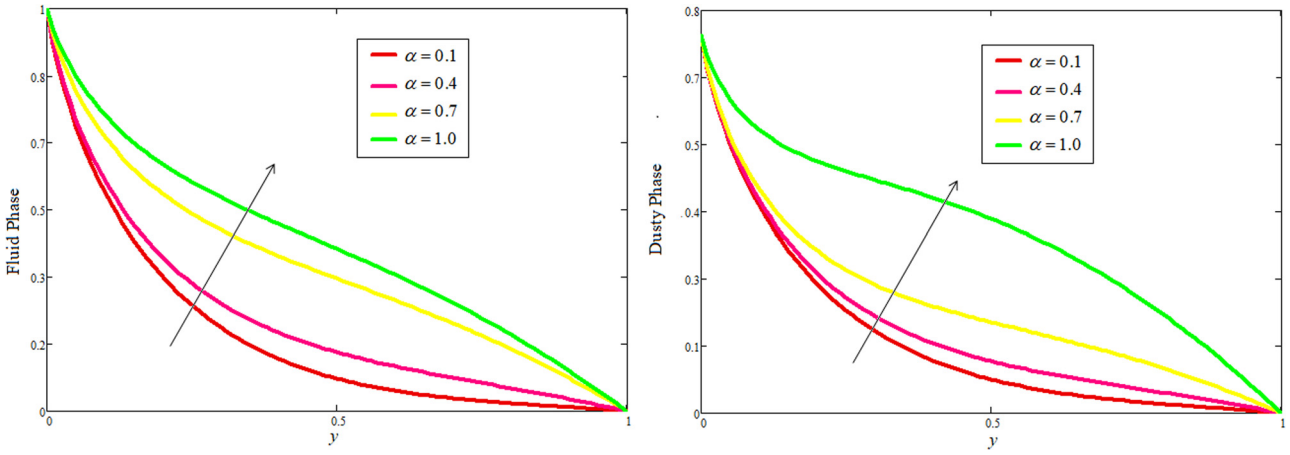

Figure 2: Effect of different values of α on $u_1(\zeta, \tau)$ and $u_2(\zeta, \tau)$.

show that using the fractional parameter yields many profiles for different fractional parameters. Fluid and dust particle velocities exhibit a crucial memory effect due to modifying fractional values, while all other parameters remain constant. Assuming that all other parameters stay the same, Figure 3(i) and (ii) exhibits the effect of changing a Casson fluid parameter on the velocity profiles of Casson and dusty fluids, respectively. When the Casson fluid parameter values increase, the viscous forces become more important than the thermal forces, which tend to reduce the velocities of both fluids. Figure 4(i) and (ii) shows the effect of the Grashof number on the velocity distributions of Casson fluid and dust particles, respectively. Findings show that the buoyancy forces increase with the Grashof number, leading to higher velocities for the Casson and dusty fluids. The correlation between dust particle density and temperature is the subject of this study. Assuming a spherical form, Stock's drag force shows that as the dusty parameter increases, the viscous forces of viscoelasticity increase. Figure 5(i) and (ii) makes it abundantly evident that when there is an increase in the total number of dust particles, there is also an increase in the overall velocity of the fluid as well as the dusty fluid. In Figure 6(i) and (ii), we can observe how the magnetic parameter influences the velocities of the Casson fluid and the dust particles, respectively. When the magnetic parameter increases, the velocities of both fluids and dusty fluids decrease. Because increasing values of the magnetic parameter increase the frictional forces on the flow of fluid, known as Lorentz forces, the thickness of the momentum boundary barrier is reduced, which results in slowing of both velocities. This phenomenon may be explained by a physical phenomenon known as the Lorentz force. The influence of the dusty fluid parameter on the velocity profiles of dust particles and Casson fluid, respectively, is shown in Figure 7(i) and (ii), which provides a summary of the effect. Because of the

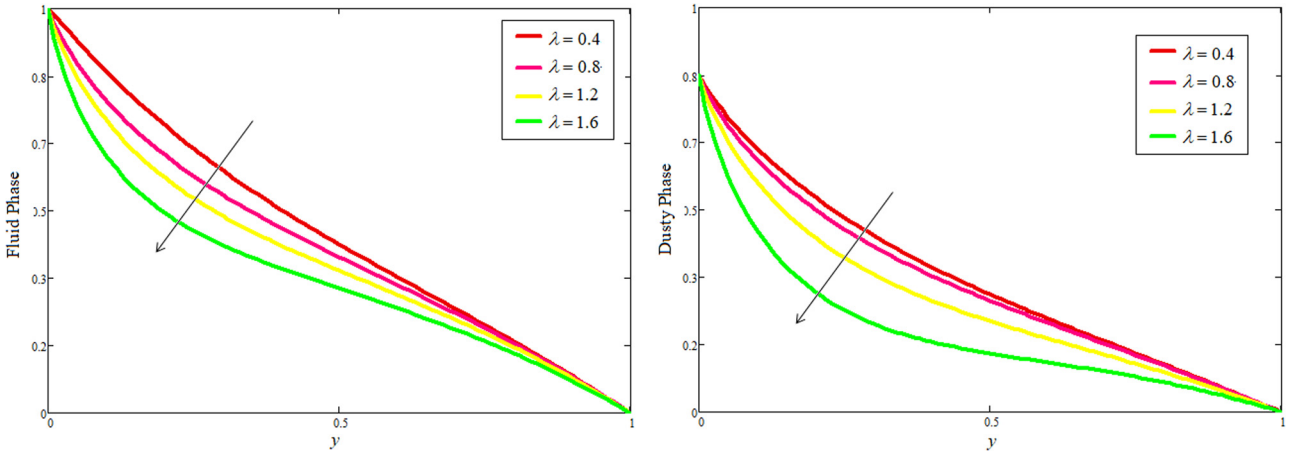

Figure 3: Effect of different values of λ on $u_1(\zeta, \tau)$ and $u_2(\zeta, \tau)$.

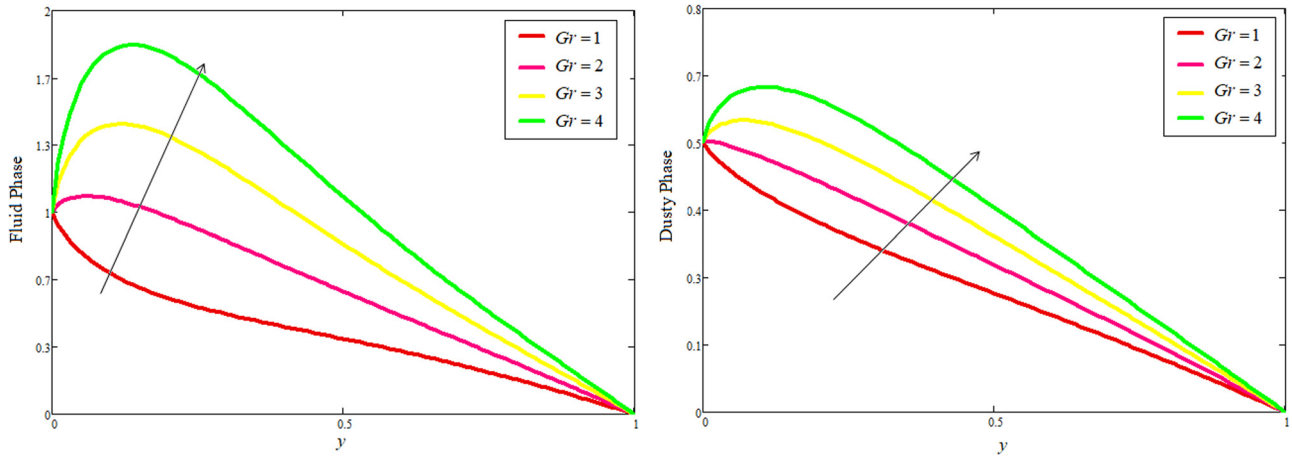

Figure 4: Effect of different values of Gr on $u_1(\zeta, \tau)$ and $u_2(\zeta, \tau)$.

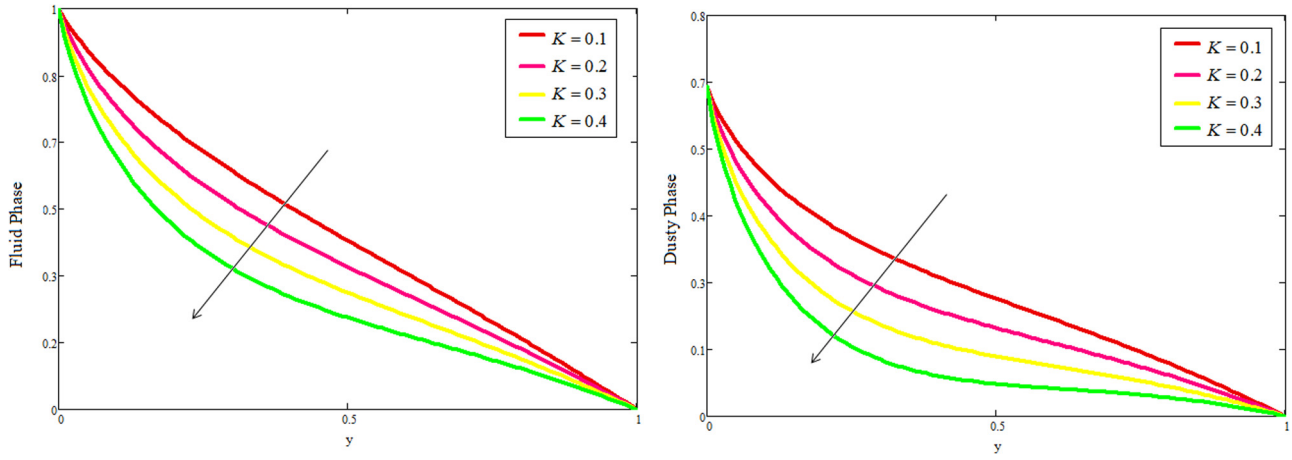

Figure 5: Effect of different values of K on $u_1(\zeta, \tau)$ and $u_2(\zeta, \tau)$.

inverse connection that exists between the dusty fluid parameter and the dust particle mass, an increase in the dusty fluid parameter results in a decrease in the dust particle mass, which in turn leads to an increase in both the Casson velocity and the dusty fluid velocity. Figure 8(i) and (ii) shows the influence that the Reynolds number has

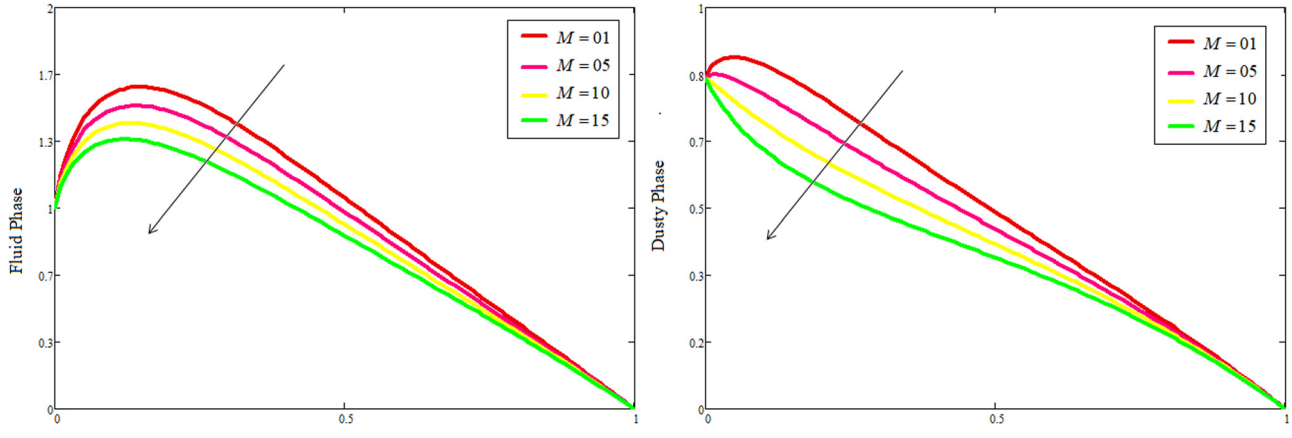

Figure 6: Effect of different values of M on $u_1(\zeta, \tau)$ and $u_2(\zeta, \tau)$.

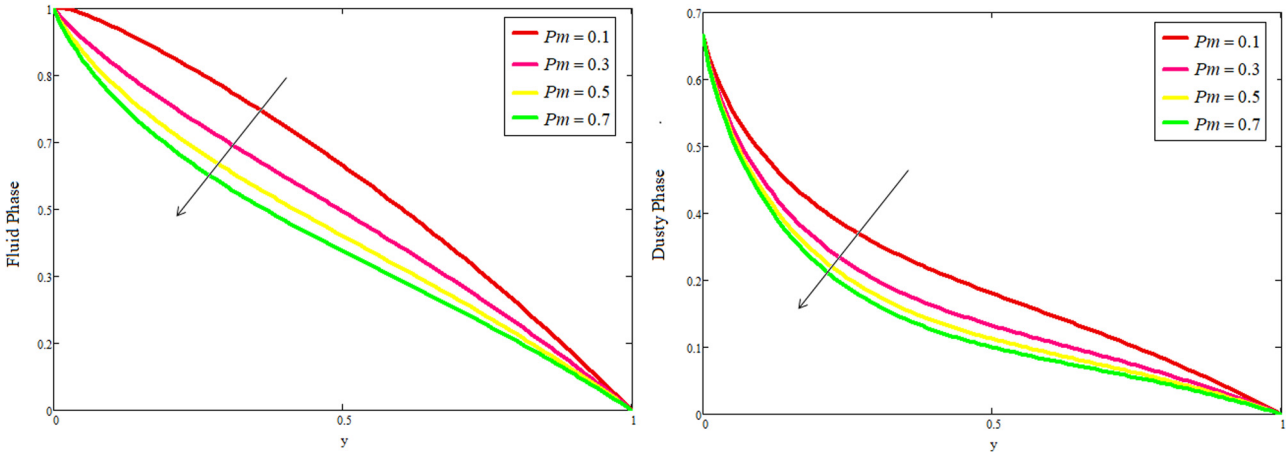

Figure 7: Effect of different values of Pm on $u_1(\zeta, \tau)$ and $u_2(\zeta, \tau)$.

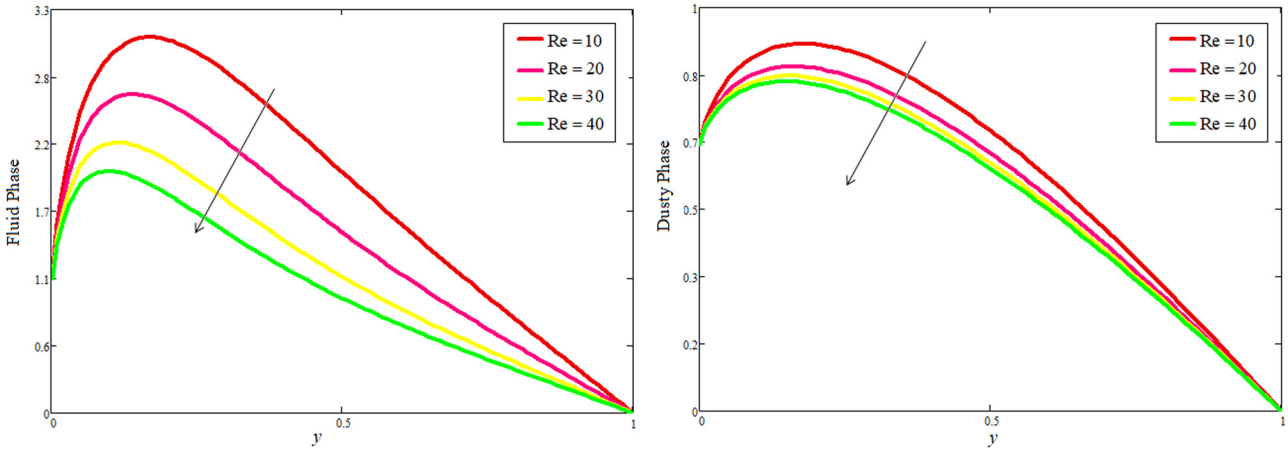

Figure 8: Effect of different values of Re on $u_1(\zeta, \tau)$ and $u_2(\zeta, \tau)$.

on the fluid velocity and dust particle velocity profiles, respectively. The inertial forces acting on the fluid rise in proportion to the Reynolds number; as a result, the velocity profiles in both directions experience a reduction in speed. Figure 9(i) and (ii) illustrates the influence of the volume fraction parameter on the velocity of the tetra-hybrid nanofluid and dust particles, respectively. The tetra-hybrid nanofluid and dust particle velocity profiles drop as the volume fraction of the tetra-hybrid nanofluid rises, which indicates that the tetra-hybrid nanoparticles are physically slowing the flow of the fluid. The greater concentration of tetra-hybrid nanoparticles results in the generation of resistive forces, which cause the nanoparticles to travel at a more leisurely pace inside the channel. When there is a higher concentration of fluid, the viscosity of the tetra-hybrid nanofluid increases, which results in a reduction in the velocity profiles of both the tetra-hybrid nanofluid and the dust particles.

Figure 10(i) and (ii) provides a comparison of tetra-nanofluid with tri-nanofluid, hybrid nanofluid, nanofluid, and classical fluid in terms of the velocity profile. When compared to tri-nanofluid, hybrid nanofluid, nanofluid, and classical fluid, Figure 10 makes it abundantly evident that tetra-nanofluid can adjust the velocity boundary layer more swiftly.

Figure 11 shows the effects of volume fraction on the temperature distribution. The temperature of the fluid rises as volume friction or viscous heating increases. This is because the heat produced by viscous heating is dispersed throughout the fluid, raising the overall temperature of fluid. As the volume friction increases, the internal temperature distribution of fluid may become more uniform. In conclusion, increased volume friction or viscous heating in a fluid can increase the temperature distribution of fluid.

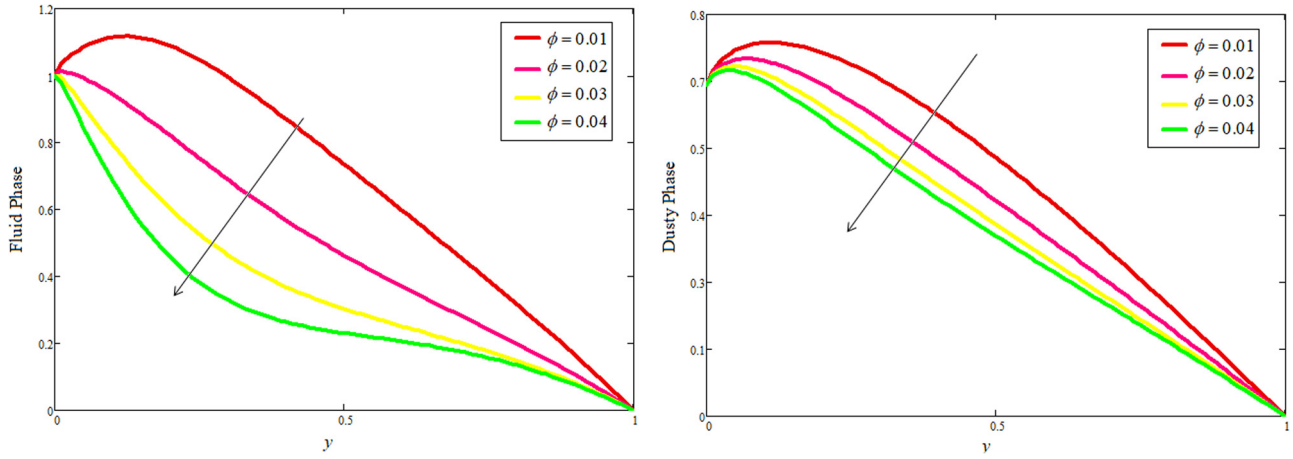

Figure 9: Effect of different values of ϕ on $u_1(\zeta, \tau)$ and $u_2(\zeta, \tau)$.

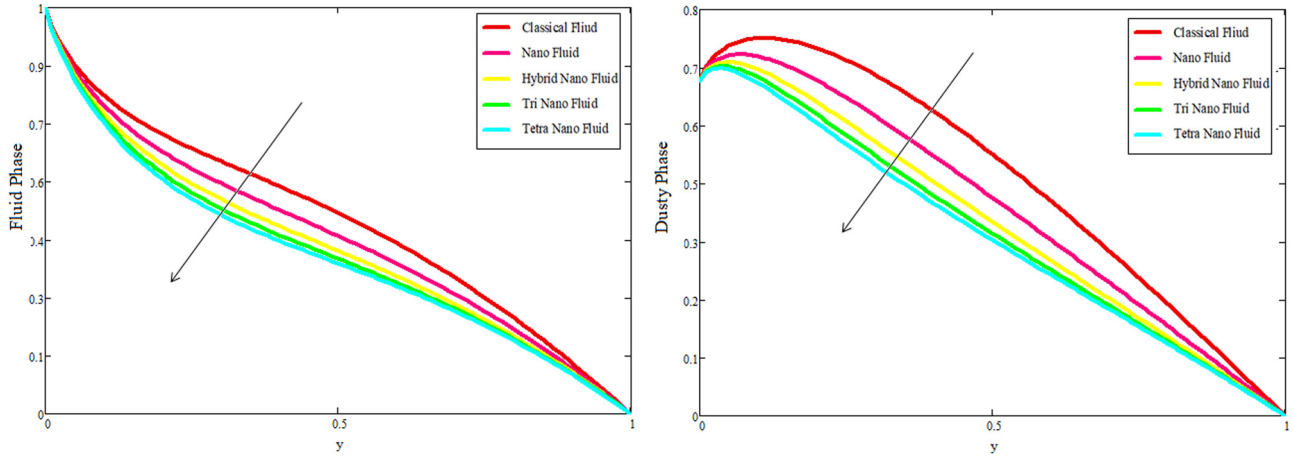

Figure 10: Comparison of tetra-nanofluid with tri-nanofluid, hybrid nanofluid, nanofluid, and classical fluid of both the velocities.

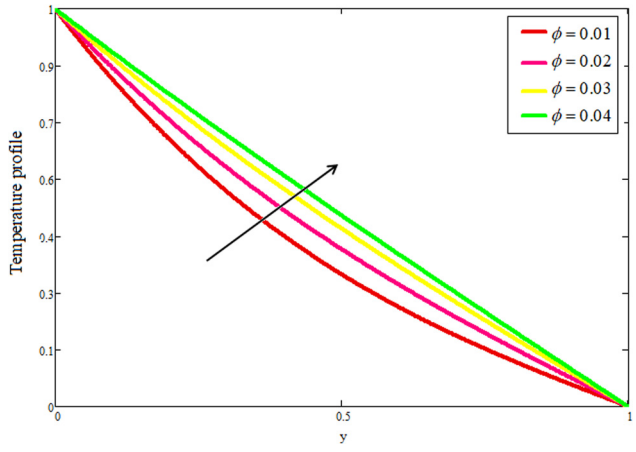

Figure 11: Effect of different values of ϕ on $\theta(\zeta, \tau)$.

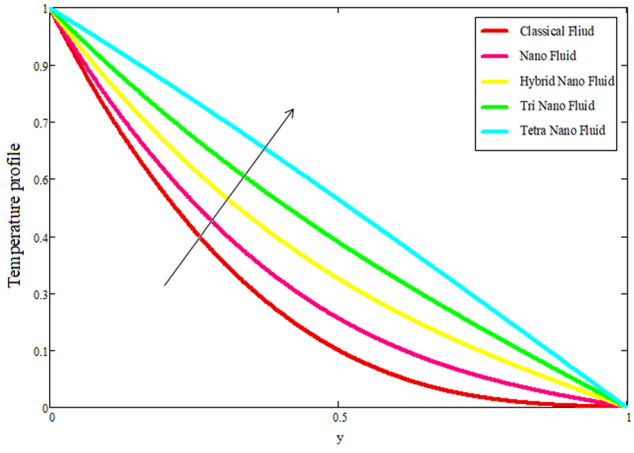

Figure 12: Comparison of tetra-nanofluid with tri-nanofluid, hybrid nanofluid, nanofluid, and classical fluid on $\theta(\zeta, \tau)$.

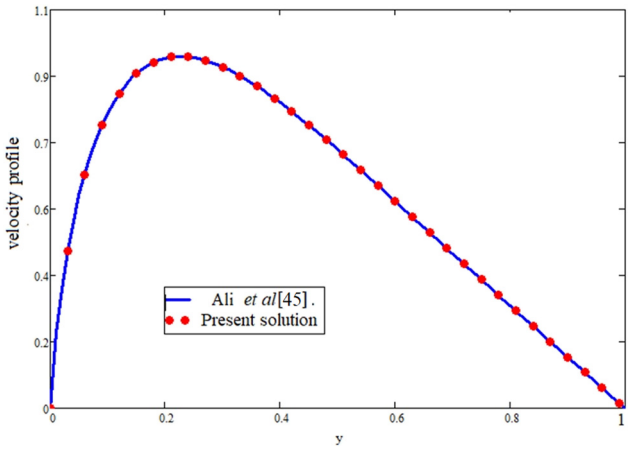

Figure 13: Comparison of this study with Ali *et al.* [45].

Table 1: Variation of Nu

t	α	ϕ	Nu
1	0.1	0.01	0.953
1.5	0.1	0.01	0.890
1	0.2	0.01	0.973
1	0.3	0.01	0.921
1	0.1	0.02	0.991
1	0.1	0.03	1.005

Table 2: Variation of Cf

t	α	λ	K	Re	Pe	Gr	Pm	M	ϕ	Cf
0.5	0.5	1	0.5	10	40	5	0.5	0.5	0.01	0.060
1.0	0.5	1	0.5	10	40	5	0.5	0.5	0.01	0.112
1.5	0.5	1	0.5	10	40	5	0.5	0.5	0.01	0.254
0.5	0.7	1	0.5	10	40	5	0.5	0.5	0.01	0.654
0.5	0.8	1	0.5	10	40	5	0.5	0.5	0.01	0.543
0.5	0.5	2	0.5	10	40	5	0.5	0.5	0.01	0.126
0.5	0.5	3	0.5	10	40	5	0.5	0.5	0.01	0.415
0.5	0.5	1	1.0	10	40	5	0.5	0.5	0.01	0.456
0.5	0.5	1	1.5	10	40	5	0.5	0.5	0.01	1.002
0.5	0.5	1	0.5	20	40	5	0.5	0.5	0.01	0.710
0.5	0.5	1	0.5	30	40	5	0.5	0.5	0.01	0.973
0.5	0.5	1	0.5	10	50	5	0.5	0.5	0.01	0.774
0.5	0.5	1	0.5	10	60	5	0.5	0.5	0.01	0.925
0.5	0.5	1	0.5	10	40	10	0.5	0.5	0.01	0.119
0.5	0.5	1	0.5	10	40	15	0.5	0.5	0.01	1.204
0.5	0.5	1	0.5	10	40	5	0.6	0.5	0.01	0.922
0.5	0.5	1	0.5	10	40	5	0.7	0.5	0.01	1.176
0.5	0.5	1	0.5	10	40	5	0.5	1.0	0.01	0.209
0.5	0.5	1	0.5	10	40	5	0.5	2.0	0.01	1.259
0.5	0.5	1	0.5	10	40	5	0.5	0.5	0.02	0.109
0.5	0.5	1	0.5	10	40	5	0.5	0.5	0.03	1.025

Table 3: Comparison of tetra-nanofluid with tri-nanofluid, hybrid nanofluid, nanofluid, and classical fluid

Fluid name	Nu	Percentage
Classical fluid	0.842	
Nanofluid	0.942	11.8764
Hybrid nanofluid	1.019	21.0213
Tri-nanofluid	1.096	30.1662
Tetra-nanofluid	1.173	39.3111

Figure 12 shows the comparison of tetra-hybrid nanofluid with tri-nanofluid, hybrid nanofluid, nanofluid, and classical fluid temperature profiles. It is clear from Figure 12 that adding tetra-hybrid nanofluid to the base fluid enhances the heat transfer as compared to tri-nanofluid, hybrid nanofluid, nanofluid, and classical fluid. Our current solution is reduced to Ali *et al.'s* [45] solution in the absence of tetra-hybrid nanofluids. Both solutions overlap, demonstrating the correctness and validity of our present solutions (Figure 13).

A dimensionless measure of convective heat transmission is the Nusselt number (Nu). It is a measurement of the boundary-layer heat transfer efficiency (convective to conductive). The fluid characteristics, the solid surface properties, and the flow circumstances are all factors that influence the Nusselt number.

Table 1 displays the fluctuation of the Nusselt number (Nu) *versus* ϕ, α, and t. It has been noted that raising the value of ϕ increases the value of Nu. When the value of ϕ decreases, the values of α and t increase.

In order to optimize heat transmission in a variety of engineering environments, it is crucial to understand how these characteristics impact the Nusselt number.

Skin friction is a phenomenon in fluid dynamics that explains the frictional force between a fluid and a solid surface. The skin friction force relies on the fluid viscosity, velocity, surface roughness, and object size and form. The skin friction for laminar flow (low Reynolds number) is directly proportional to the viscosity and velocity of fluid,

Table 4: Thermophysical properties

Material	Base fluids	Nanoparticles			
	SA	Cu	Al_2O_3	Ag	TiO_2
ρ (kg/m^3)	989	8,933	3,970	10,500	4,250
c_p (J/kg K)	4,175	385	765	235	686.2
K (W/m K)	0.613	401	40	429	8.9528
$\beta \times 10^{-5}$ (K^{-1})	0.99	1.67	0.85	1.89	0.9

but for turbulent flow (high Reynolds number), it depends on the surface roughness and the size and form of object.

The various factors and their impacts on skin friction are shown in Table 2. It should be brought to reader's attention that the high values of t, α , and Gr are decreasing. Skin friction is vital for designing aircraft wings, ship hulls, and pipelines that move through fluids. Reducing skin friction improves fluid movement and energy efficiency. Smoothing the surface, utilizing low-friction coatings or materials, and regulating fluid flow to reduce turbulent boundary layers reduce skin friction.

Table 3 shows the Nu comparison of tetra-nanofluid with tri-nanofluid, hybrid nanofluid, nanofluid, and classical fluid. It is clear from Table 3 that the value of heat transfer rate (Nu) enhanced from 0 to 39.3111%. Table 4 shows the thermophysical properties of the base fluid and suspended nanoparticles.

5 Conclusions

The purpose of this study is to analyze the generalized natural convection flow of Casson dusty fluid and tetra-hybrid nanofluid between vertical plates that have varying temperatures. The model is fractionalized using a method known as CF time-fractional derivative, which does not require a single kernel. Laplace and FSFT approaches are then used to solve the set of controlling PDEs, using the MATHCAD 15 program. The following is a condensed version of the most important results from this investigation:

- The generalized Casson fluid model provides a more accurate representation of fluid behavior by depicting the velocity profile in fluid, as demonstrated by graphical findings.
- The heat transfer rate enhanced from 0 to 39.3111% by adding tetra-hybrid nanofluid.
- The fluid velocity and the particle velocity enhance with the enhancement of α and Gr.
- By increasing the values of M, both the velocities show the reducing behavior.
- The high value of ϕ results in an increasing temperature profile.
- Casson dusty fluids and tetra-hybrid nanofluids are only two examples of complicated phenomena used extensively in engineering and industrial applications. One such use is the use of dusty fluids in gas-freezing systems and nuclear power reactors.

Finally, the authors would like to make some recommendations for further study to the readers, which are listed in the following:

- The following concept can be applied to more complex geometries such as wedges and cones.
- One approach is used to investigate the same idea for several types of fluids with more physical conditions.
- In addition, several novel fractional derivatives may be used to more efficiently summarize existing fluid models and concentration equations.

Acknowledgments: The authors extend their appreciation to the Deanship of Scientific Research at King Khalid University for funding this work through large group research project under grant number (RGP2/89/44).

Funding information: This work was funded through large group research project under grant number (RGP2/89/44) by the Deanship of Scientific Research at King Khalid University.

Author contributions: All authors have accepted responsibility for the entire content of this manuscript and approved its submission.

Conflict of interest: The authors state no conflict of interest.

Data availability statement: All data generated or analysed during this study are included in this published article.

References

[1] Dash RK, Mehta KN, Jayaraman G. Casson fluid flows in a pipe filled with a homogeneous porous medium. Int J Eng Sci. 1996;34(10):1145–56.

[2] Oka S. An approach to α unified theory of the flow behavior of time-independent non-Newtonian suspensions. Japanese J Appl Phys. 1971;10(3):287.1–5.

[3] Mukhopadhyay S, Mandal IC. Boundary layer flow and heat transfer of a Casson fluid past an asymmetric porous wedge with surface heat flux. Chin Phys B. 2014;23(4):044702–12.

[4] Kim S. A study of non-Newtonian viscosity and yield stress of blood in a scanning capillary-tube rheometer. (Doctoral dissertation, Drexel University); 2002.

[5] Akbar NS, Khan ZH. The metachronal beating of cilia under the influence of Casson fluid and magnetic field. J Magnetism Magnetic Mater. 2015;378:320–6.

[6] Akbar NS. Influence of magnetic field on peristaltic flow of a Casson fluid in an asymmetric channel: application in crude oil refinement. J Magnetism Magnetic Mater. 2015;378:463–8.

[7] Noreen SA, Butt AW. Physiological transportation of Casson fluid in a plumb duct. Commun Theor Phys. 2015;63(3):347–57.

[8] Asjad MI, Usman M, Kaleem MM, Baleanu D, Muhammad T. Thermal transport with nanoparticles of fractional Oldroyd-B fluid under the effects of magnetic field, radiations, and viscous

dissipation: Entropy generation; via finite difference method. Open Phys. 2022;20(1):1216–32.
[9] Nadeem S, Haq RU, Akbar NS. MHD three-dimensional boundary layer flow of Casson nanofluid past a linearly stretching sheet with convective boundary condition. IEEE Trans Nanotechnol. 2014;13(1):109–15.
[10] Khan D, Khan A, Khan I, Ali F, Karim FU, Tlili I. Effects of a relative magnetic field, chemical reaction, heat generation, and Newtonian heating on convection flow of Casson fluid over a moving vertical plate embedded in a porous medium. Sci Rep. 2019;9(1):1–18.
[11] Reza-E-Rabbi S, Arifuzzaman SM, Sarkar T, Khan MS, Ahmmed SF. Explicit finite difference analysis of an unsteady MHD flow of a chemically reacting Casson fluid past a stretching sheet with Brownian motion and thermophoresis effects. J King Saud Univ Sci. 2020;32(1):690–701.
[12] Rana BMJ, Arifuzzaman SM, Islam S, Reza-E-Rabbi S, Al-Mamun A, Mazumder M, et al. Swimming of microbes in blood flow of nano-bioconvective Williamson fluid. Therm Sci Eng Prog. 2021;25:101018.
[13] Faisal M, Mabood F, Asogwa KK, Badruddin IA. On convective heat and mass transport of radiative double diffusive Williamson hybrid nanofluid by a Riga surface. Int J Mod Phys C. 2023;34(8):2350111.
[14] Asogwa KK, Mebarek-Oudina F, Animasaun IL. Comparative investigation of water-based Al2O3 nanoparticles through water-based CuO nanoparticles over an exponentially accelerated radiative Riga plate surface via heat transport. Arab J Sci Eng. 2022;47(7):8721–38.
[15] Taylor R, Coulombe S, Otanicar T, Phelan P, Gunawan A, Lv W, et al. Small particles, big impacts: A review of the diverse applications of nanofluids. J Appl Phys. 2013;113(1):1.
[16] Asogwa KK, Goud BS, Shah NA, Yook SJ. Rheology of electromagnetohydrodynamic tangent hyperbolic nanofluid over a stretching riga surface featuring Dufour effect and activation energy. Sci Rep. 2022;12(1):14602.
[17] Asogwa KK, Rajendra Prasad KC, Kumar R, Murtugudde G, Punith Gowda RJ. Transient electromagnetohydrodynamic Nanofluid flow traveling through a moving Riga plate subject to radiation and heat absorption. Int J Mod Phys B. 2022;37(17):2350168.
[18] Ramesh K, Asogwa KK, Oreyeni T, Reddy MG, Verma A. EMHD radiative titanium oxide-iron oxide/ethylene glycol hybrid nanofluid flow over an exponentially stretching sheet. Biomass Convers Biorefinery. 2023;2023:1–10.
[19] Bilal S, Asjad MI, Haq SU, Almusawa MY, Tag-ElDin EM, Ali F. Significance of Dufour and Soret aspects on dynamics of water based ternary hybrid nanofluid flow in a 3D computational domain. Sci Rep. 2023;13(1):4190.
[20] Adnan Abbas W, Bani-Fwaz MZ, Kenneth Asogwa K. Thermal efficiency of radiated tetra-hybrid nanofluid [(Al2O3-CuO-TiO2-Ag)/water] tetra under permeability effects over vertically aligned cylinder subject to magnetic field and combined convection. Sci Prog. 2023;106(1):00368504221149797.
[21] Asogwa KK, Singh Gill H, Prasannakumara BC, Madhukesh JK. Effect of thermophoretic particle deposition on the three-dimensional flow of nanofluid induced by a nonlinear stretched surface. Waves Random Complex Media. 2023;2023:1–17.
[22] Zayan M, Rasheed AK, John A, Muniandi S, Faris A. Synthesis and characterization of novel ternary hybrid nanoparticles as thermal additives in H_2O; 2021.
[23] Sajid T, Jamshed W, Eid MR, Altamirano GC, Aslam F, Alanzi AM, et al. Magnetized Cross tetra hybrid nanofluid passed a stenosed artery with nonuniform heat source (sink) and thermal radiation: Novel tetra hybrid Tiwari and Das nanofluid model. J Magn Magn Mater. 2023;569:170443.
[24] Li N, Kang G, Liu H, Li M, Qiu W, Wang Q, et al. Hybrid nanoparticles based on novel Schiff Base for durable flame retardant and antibacterial properties. Compos Part B: Eng. 2022;238:109905.
[25] Iliyasu AM, Fouladinia F, Salama AS, Roshani GH, Hirota K. Intelligent measurement of void fractions in homogeneous regime of two phase flows independent of the liquid phase density changes. Fractal Fract. 2023;7(2):179.
[26] Chen Y, Yang KS, Chang YJ, Wang CC. Two-phase pressure drop of air–water and R-410A in small horizontal tubes. Int J Multiph flow. 2001;27(7):1293–9.
[27] Banowski M, Beyer M, Szalinski L, Lucas D, Hampel U. Comparative study of ultrafast X-ray tomography and wire-mesh sensors for vertical gas–liquid pipe flows. Flow Meas Instrum. 2017;53:95–106.
[28] Salgado CM, Dam RS, Puertas EJ, Salgado WL. Calculation of volume fractions regardless scale deposition in the oil industry pipelines using feed-forward multilayer perceptron artificial neural network and MCNP6 code. Appl Radiat Isotopes. 2022;185:110215.
[29] Al-Lababidi S, Addali A, Yeung H, Mba D, Khan F. Gas void fraction measurement in two-phase gas/liquid slug flow using acoustic emission technology. J Vib Acoust. 2009;131(6):064501–(1–7).
[30] Abdulkadir M, Hernandez-Perez V, Lowndes IS, Azzopardi BJ, Brantson ET. Detailed analysis of phase distributions in a vertical riser using wire mesh sensor (WMS). Exp Therm Fluid Sci. 2014;59:32–42.
[31] Koyama S, Lee J, Yonemoto R. An investigation on void fraction of vapor–liquid two-phase flow for smooth and microfin tubes with R134a at adiabatic condition. Int J Multiph Flow. 2004;30(3):291–310.
[32] Yang HC, Kim DK, Kim MH. Void fraction measurement using impedance method. Flow Meas Instrum. 2003;14(4–5):151–60.
[33] Bhatti MM, Zeeshan A, Ellahi R, Shit GC. Mathematical modeling of heat and mass transfer effects on MHD peristaltic propulsion of two-phase flow through a Darcy-Brinkman-Forchheimer porous medium. Adv Powder Technol. 2018;29(5):1189–97.
[34] Yu X, Yi D, Huang Y, Lu Y, Roskilly AP. Experimental investigation of two-phase flow and heat transfer performance in a cooling gallery under forced oscillation. Int J Heat Mass Transf. 2019;132:1306–18.
[35] Shah NA, Vieru D, El-Zahar ER. An analytical study of the unsteady nonlinear convection flow of nanofluids in an infinitely rectangular channel. Waves Random Complex Media. 2022;2022:1–19.
[36] Nonnenmacher TF, Metzler R. On the Riemann-Liouville fractional calculus and some recent applications. Fractals. 1995;3(03):557–66.
[37] Jiang S, Zhang J, Zhang Q, Zhang Z. Fast evaluation of the Caputo fractional derivative and its applications to fractional diffusion equations. Commun Comput Phys. 2017;21(3):650–78.
[38] Cruz–Duarte JM, Rosales–Garcia J, Correa–Cely CR, Garcia–Perez A, Avina–Cervantes JG. A closed form expression for the Gaussian–based Caputo–Fabrizio fractional derivative for signal processing applications. Commun Nonlinear Sci Numer Simul. 2018;61:138–48.
[39] Goufo EFD. Application of the Caputo-Fabrizio fractional derivative without singular kernel to Korteweg-de Vries-Burgers equation*. Math Model Anal. 2016;21(2):188–98.

[40] Caputo M, Fabrizio M. Applications of new time and spatial fractional derivatives with exponential kernels. Progr Fract Differ Appl. 2016;2(2):1–11.
[41] Asjad MI, Usman M, Assiri TA, Ali A, Tag-ElDin EM. Numerical investigation of fractional Maxwell nano-fluids between two coaxial cylinders via the finite difference approach. Front Mater. 2023;9:1050767.
[42] Asjad MI, Karim R, Hussanan A, Iqbal A, Eldin SM. Applications of fractional partial differential equations for MHD Casson fluid flow with innovative ternary nanoparticles. Processes. 2023;11(1):218.
[43] Khan D, Kumam P, Watthayu W. Multi-generalized slip and ramped wall temperature effect on MHD Casson fluid: second law analysis. J Therm Anal Calorim. 2022;147(23):13597–609.
[44] Khan D, Kumam P, Watthayu W, Yassen MF. A novel multi fractional comparative analysis of second law analysis of MHD flow of Casson nanofluid in a porous medium with slipping and ramped wall heating. ZAMM-J Appl Math Mechanics/Zeitschrift für Angew Mathematik Mechanik. 2023;103(6):e202100424.
[45] Ali G, Ali F, Khan A, Ganie AH, Khan I. A generalized magnetohydrodynamic two-phase free convection flow of dusty Casson fluid between parallel plates. Case Stud Therm Eng. 2022;29:101657.

Appendix

$$n_4 = (\mathrm{Re}c_1n_0n_1n_2 - M\ b_1 + K)(n_2(\mathrm{Re}c_1n_0 + M))^{-1},$$

$$n_5 = (K\ n_1 - Mn_2n_1n_3n_2)(\mathrm{Re}c_1n_0 + M)^{-1},\ n_6 = \frac{\mathrm{Gr}A_1}{n_2^{-1}},$$

$$b_1 = n_2(n_1 + n_3),\ b_2 = n_0n_1n_2,\ b_3 = n_1n_2n_3,\ b_4 = n_0n_2n_3,$$
$$b_5 = n_1n_4\ ,\ b_6 = n_1n_5n_6,\ b_7 = n_0n_2,$$

$$A_4 = (\mathrm{Re}c_1n_0n_2n_3 + \lambda_1c_2(n\pi)^2b_1 - n_1^2K - Mb_1)(\mathrm{Re}c_1b_7 + \lambda_1c_2(n\pi)^2n_2 - K - M\ n_2)^{-1},$$

$$A_5 = (\lambda_1c_2(n\pi)^2b_5 - b_6K - Mb_5)(\mathrm{Re}c_1b_7 + \lambda_1c_2(n\pi)^2n_2 - K - M\ n_2)^{-1},$$

$$A_6 = \frac{A_4 - \sqrt{A_4^2 - 4A_5}}{2},\ A_7 = \frac{A_4 + \sqrt{A_4^2 - 4A_5}}{2},\ A_8 = n_4 + n_5A_6 - A_6^2\frac{1}{A_6 + A_7}\ ,\ A_9 = \frac{A_7^2 + n_5A_7 - n_4}{A_6 + A_7}, A_{10} = \frac{n_6n_1^2n_3}{A_2A_6A_7},$$

$$A_{11} = \frac{n_6(n_1^2n_3(A_2A_7 - A_2A_6 + A_6A_7) - A_2A_6A_7(n_1^2 + 2n_1n_3))}{(A_2A_6A_7)^2},$$

$$A_{12} = \frac{n_6(n_1n_3(n_1 - 2A_1) + A_2^2(n_3 - 2n_1 - 1) - n_1^2A_7)}{A_2^2(A_2 - A_6)(A_2 - A_7)},$$

$$A_{13} = \frac{n_6(n_1n_3(n_1 - 2A_7) + A_7^2(n_3 + 2n_1 - 1) - n_1^2A_6)}{A_6^2(A_6 - A_2)(A_6 + A_7)},$$

$$A_{14} = \frac{n_6(n_1n_3(n_1 + 2A_7) + A_7^2(n_3 + 2n_1 + 1) + n_1^2A_7)}{A_7^2(A_2 + A_7)(A_6 + A_7)}.$$